Bioinspired 3D penetrating structured micro-mesoporous NiCoFe-LDH@ZnIn$_2$S$_4$ Z-scheme heterojunction for simultaneously photocatalytic H$_2$ evolution coupled with benzylamine oxidation

Chenxi Tang [a], Tengfei Bao [a], Shuming Li [a], Xiuyan Wang [b], Heng Rao [a], Ping She [a,*], Jun-sheng Qin [a]

[a] *State Key Laboratory of Inorganic Synthesis and Preparative Chemistry, College of Chemistry, International Center of Future Science, Jilin University, 2699 Qianjin Street, Changchun 130012, PR China*
[b] *Key Laboratory of Bionic Engineering (Ministry of Education), College of Biological and Agricultural Engineering, Jilin University, 5988 Renmin Street, Changchun 130012, PR China*

ARTICLE INFO

ABSTRACT

Metal sulfides have attracted extensive attention in photocatalysis, but are limited by the high combination rate of photo-induced charges due to their bulky structures. Herein, a bioinspired three-dimensional (3D) penetrating structured micro-mesoporous Z-scheme heterojunction of NiCoFe-layered double hydroxides@ZnIn$_2$S$_4$ (NiCoFe-LDH@ZIS) with S vacancies was constructed. The NiCoFe-LDH@ZIS heterojunction was prepared by limiting the growth of ZIS through intercalating flower-like ZIS within dandelion-like LDH. The obtained NiCoFe-LDH@ZIS demonstrated a superior photocatalytic H$_2$ evolution (PHE) rate (113.57 mmol g^{-1} h^{-1}) and 97.78 % conversion rate of benzylamine oxidation, simultaneously. This superior photocatalytic performance benefits from the enhanced charge separation induced by the combination of 3D penetrating micro-mesoporous structure, the introduction of S vacancies, and Z-scheme heterojunction. This dimensional-matched 3D penetrating porous heterojunction affords more abundant active sites, accelerated separation of photogenerated carriers, and reduced activation energy of H$_2$ evolution. This unique structure provides a feasible reference for bi-functional photocatalytic reactions.

1. Introduction

Hydrogen energy is recognized as an essential clean energy source, which possesses great possibility to address energy scarcity and environmental pollution [1]. PHE can continuously convert sunlight into hydrogen energy through photocatalysis. The whole photocatalytic process does not produce any pollutants, which is consistent with the current sustainable development concept of carbon neutrality [2]. However, PHE is often restricted by easily combined photogenerated electron-hole pairs (PEHP) and slow kinetics of the reaction in water oxidative half-reaction [3,4]. It is often necessary to add hole scavengers such as diethanolamine, triethanolamine (TEOA), ethanol, and ethylenediamine to the reaction [5]. These sacrificial electron donors (SEDs) can eliminate photoinduced holes, which in turn promote the reductive half-reaction for hydrogen generation based on the photoinduced electrons [6]. Introducing harmful organic scavengers for photoinduced

holes will raise the cost and introduce extra waste or pollution. Therefore, it is urgent to develop efficient and green bifunctional photocatalysts for H$_2$ evolution and organic oxidation simultaneously. Imines are nitrogen-containing organic compounds with biological activity, which are often synthesized through the organic synthesis approaches [3]. In recent years, imines can be obtained by combining the PHE process and oxidative coupling of benzylamines simultaneously [4]. The bifunctional processes can obtain clean hydrogen and high-value chemicals in one photocatalytic redox reaction process.

As a common semiconductor photocatalyst, ZIS has garnered a large amount of notice in recent years, which possesses strong light harvesting ability, low toxicity, and is easy to prepare [7–9]. Nevertheless, the photocatalytic property of bulky ZIS is still limited to the low interfacial reaction rate and easy recombination of photogenerated carriers [10]. Fortunately, controlling the morphology of ZIS and constructing heterostructures are feasible approaches to enhance its PHE performance.

---

* Corresponding author.
 E-mail address: sheping@jlu.edu.cn (P. She).

The nanomorphology of ZIS such as 0D (quantum dots and nanoparticles), 1D (nanowires, nanoribbons and nanotubes), 2D (nanosheets) and 3D (flowers and microspheres) has a remarkable influence on their photocatalytic property [11]. The hierarchical nanostructure can improve sunlight utilization efficiency and provide more active sites by increasing surface areas, which will increase the activity of photocatalysts [12]. 2D nanosheet-structured ZIS often demonstrates enhanced specific surface area with more active sites, which makes it easy to form heterogeneous structures with other semiconductor materials. The ultrathin 2D nanosheets can facilitate the migration of photogenerated charges, resulting in longer photogenerated electron lifetimes and in turn enhanced photocatalytic activity [13]. Compared with conventional 2D nanosheet-structured ZIS, 3D hierarchical structured ZIS can improve the adsorption capacity to a much higher extent [14]. Upon light irradiation, the light absorption efficiency of heterogeneous materials would be increased according to the elongated light transmission distance induced by multi-layer scattering [15]. Xing et al. [16] prepared Mo-doped ZIS flower-like hollow microspheres (M-ZIS) by hydrothermal method. The PHE rate of M-ZIS reaches up to 4.62 mmol g^{-1} h^{-1}, which is much higher than bulk ZIS. The increased PHE activity is due to the 3D hollow microsphere structure, which assures sufficient light absorption and exposes more active sites. Moreover, Xu et al. [8] synthesized binary nickel-modified ZIS nanoflowers by the photodeposition method, which demonstrated superior bi-functional photocatalytic activity for PHE (1.46 mmol g^{-1} h^{-1}) and selective oxidation of alcohol. Shi et al. [17] similarly created 3D hierarchical ZIS rich in In vacancies, which exhibited higher CO_2 photoreduction efficiency (CO evolution rate: 298 μmol g^{-1} h^{-1}) than pristine ZIS. Therefore, 3D morphology and vacancies have a great advantage for ZIS-based photocatalysis, but ZIS with penetrating mesopores is rarely reported.

Among various types of heterojunctions, Z-scheme heterojunctions can facilitate charge separation and preserve a high redox potential for holes and electrons, thus facilitating photocatalytic redox reactions [18, 19]. Li et al. [20] constructed the piezoelectric and hierarchical Z-scheme heterostructure of BaTiO$_3$ @ZIS without any co-catalyst, which demonstrated a high PHE efficiency (8041 μmol g^{-1}) and C-N coupling products of benzylamine (5593 μmol g^{-1}). Chen et al. [21] also prepared a ternary urchin-like ZIS-Au-TiO$_2$ Z-scheme composite by the solvothermal method. It achieved a much higher PHE rate (186.3 μmol g^{-1} h^{-1}) than other controls, which was ascribed to the facilitated Z-scheme charge transfer at the interface. The formation of a Z-scheme structure with spatially separated charges and higher redox ability will improve the photocatalytic efficiency of ZIS. Nevertheless, there are few reports related to ZIS-based Z-scheme heterojunction with a 3D penetrating micro-mesoporous structure.

For the modification of ZIS, the semiconductor with a low Fermi level is usually selected [22]. LDH nanomaterials have drawn great interest in photocatalysis due to their suitable energy band structure, low cost, facile preparation, tunable structure, good stability, and high redox activity [23,24]. However, the catalytic activity of LDH is restricted by the low PEHP separation rate and weak redox ability, which impede their further development in photocatalysis [25]. As a material with a lamellar structure, the introduction of LDH into the synthesis process of ZIS can influence the morphology of ZIS. This combination not only ensures the high crystallinity of ZIS but can also generate a built-in electric field inside the whole material, which accelerates the transport process of photogenerated carriers [26]. The photocatalytic activity of composites is improved based on the decreased combination centers of PEHP and the enhanced spatial carrier separation [24,25]. Xia et al. [26] successfully prepared ZIS/MgAl-LDH (LDHZIS) heterojunction through the hydrothermal method. The redox centers on LDHZIS heterojunction can attain spatial separation due to the synergies of crystal facet engineering and hole-storage layer from MgAl-LDH. It will promote charge separation and kinetics of surface reactions. LDHZIS shows excellent photocatalytic performances for Cr(VI) reduction and PHE, exceeding 5.75 times and 4.1 times more than pure ZIS, respectively.

Natural honeycomb structures are well known for their rich pore structures, unique penetration and adsorption characteristics, ultrahigh structural stability, and interconnected open channels for superior ventilation capacity [27]. Consequently, it is promising to combine the merits of ZIS nanosheets with an interconnected porous morphology, which would further improve photocatalytic efficiency. Herein, inspired by the natural honeycomb structures, we designed a 3D penetrating micro-mesoporous NiCoFe-LDH@ZIS Z-scheme heterojunction by introducing LDH to limit the growth of ZIS. The NiCoFe-LDH@ZIS catalysts are systematically evaluated by a visible light-catalyzed bifunctional photocatalysis of cooperatively PHE and benzylamine oxidation coupling reaction with no SEDs. The photocatalytic results show that NiCoFe-LDH@ZIS exhibits a superior PHE rate (113.57 mmol g^{-1} h^{-1}), which is about 6.24 times more than bulky flower-like ZIS and 82.30 times of dandelion-like NiCoFe-LDH. The conversion rate of benzylamine in the system is 97.78 % and the selectivity of N-benzylidenebenzylamine is 80.72 % by NiCoFe-LDH@ZIS, which is much greater than pristine ZIS (65.30 % and 38.45 % respectively). Furthermore, NiCoFe-LDH@ZIS demonstrated superior photostability after four cycles, the PHE performance and the selectivity and conversion rate of benzylamine oxidative coupling hardly decayed. The experimental results and DFT first-principles calculations confirm the 3D penetrating micro-mesoporous structure of NiCoFe-LDH@ZIS facilitates contact with the reactive substrate and allows greater utilization of the active center. The penetrating micro-mesoporous ensures that blockage does not occur easily after multiple cycles, while the multiple refractions of light in the pores can also enhance light utilization efficiency. Furthermore, Z-scheme heterojunctions and the introduction of S vacancies will accelerate charge separation and suppress the combination of PEHP. The 3D penetrating structured micro-mesoporous Z-scheme heterojunction photocatalysts presented here hold great potential for bifunctional photocatalysis in the future.

2. Experimental section

2.1. Materials

All chemicals were analytically pure without any further purification. Cetyltrimethylammonium bromide (CTAB) and 2-methylimidazole were from Sinopharm. Co(NO$_3$)$_2$·6 H$_2$O, Ni(NO$_3$)$_2$·6 H$_2$O, indium chloride and ferric nitrate were from Aladdin. The anhydrous zinc chloride and glycerol were purchased from Innochem. Thioacetamide (TAA), methanol and ethanol were supplied by Tianjin Guangfu.

2.2. Synthesis of ZIF-67

Typically, 340 mg of Co(NO$_3$)$_2$·6 H$_2$O and 1.56 g of 2-methylimidazole with CTAB (0.26 mg) were dissolved into DI water (5 mL), respectively. The former solution was quickly poured into the latter solution at RT (25 °C). After stirring, the resulting purple solid was washed with ethanol (3 times). And the products were dried overnight (80 °C).

2.3. Synthesis of dandelion-like NiCoFe-LDH

All of the synthesized ZIF-67 was added into 400 mL ethanol solution containing 100 mg of Fe(NO$_3$)$_3$·9 H$_2$O and 1368 mg of Ni(NO$_3$)$_2$·6 H$_2$O and refluxed at 80 °C. After 2 h, the products were finally centrifuged, washed and dried overnight (80 °C).

2.4. Synthesis of flower-like ZIS

The precursor solution of flower-like ZIS was synthesized by mixing 8 mL of H$_2$O (pH=2.5), InCl$_2$·4 H$_2$O (175.8 mg), ZnCl$_2$ (81.6 mg), TAA (90 mg) and glycerol (2 mL) under sonication for 5 min. Subsequently, the well-dispersed solution was stirred for 2 h at 80 °C. After

centrifuging, the product was washed with deionized water and dried overnight (60 °C).

2.5. Synthesis of 3D penetrating structured micro-mesoporous NiCoFe-LDH@ZIS Z-scheme heterojunction

Typically, a 3D penetrating structured micro-mesoporous NiCoFe-LDH@ZIS Z-scheme heterojunction bifunctional catalyst was prepared by intercalating flower-like ZIS within dandelion-like NiCoFe-LDH to limit the growth of ZIS. Specifically, NiCoFe-LDH@ZIS was prepared by mixing the NiCoFe-LDH with ZIS precursor solution followed by heating 2 h at 80 °C. After centrifuging, the above resultant product was washed and dried overnight at 60 °C.

2.6. Characterizations

The details of the catalyst characterizations, DFT calculation and photoelectrochemical/electrochemical characterizations are described in Supporting Information.

2.7. Photocatalytic test

The PHE coupled with the oxidation of benzylamine was performed by a 300 W Xenon lamp. Typically, 1 mg of the photocatalyst was included in a 10 mL of acetonitrile solution containing 100 μL of DI water and 100 of μL benzylamine followed by sonication. Then, the solution was transferred into a reaction bottle followed by bubble treatment with pure Ar several times to eliminate the air. The generated H_2 was tested by GC-2014. After irradiation for 8 h, the photocatalyst was removed and the liquid product after filtering was identified and quantized by the gas chromatograph-mass spectrometer (Thermo Fisher Trace ISQ).

3. Results and discussion

The 3D penetrating micro-mesoporous NiCoFe-LDH@ZIS Z-scheme heterojunction is prepared by a three-step process in Scheme 1. Firstly, ZIF-67 with dodecahedral morphology is prepared by the introduction of 2-methylimidazole and cobalt nitrate. The as-synthesized ZIF-67 (Fig. S1) is etched and in situ transforms into a dandelion-like lamellar NiCoFe-LDH in ethanol solutions containing iron nitrate and nickel nitrate (Fig. S2). The lamellar structured NiCoFe-LDH is introduced into the synthesis process of flower-like ZIS. Finally, the intercalation of LDH limited the growth of ZIS, resulting in a 3D penetrating micro-mesoporous NiCoFe-LDH@ZIS Z-scheme heterojunction. Compared

with the dandelion-like lamellar structured NiCoFe-LDH (Fig. S2) and the flower-like ZIS (Fig. S3), the TEM images of NiCoFe-LDH@ZIS (Fig. 1a) demonstrate a 3D penetrating micro-mesoporous morphology. The two lattice fringes (0.33 and 0.25 nm) in the HRTEM images correspond to ZIS (101) and NiCoFe-LDH (012) crystal planes, respectively (Fig. 1b-d) [4,23]. The coexistence of these two crystalline surfaces demonstrates the successful formation of a tightly integrated heterojunction of LDH and ZIS [20]. In Fig. 1e, the EDS pattern shows the elemental composition of NiCoFe-LDH@ZIS. A low percentage of Ni, Co, and Fe elements appear compared to the EDS pattern of pure ZIS (Fig. S4), implying the successful combination of ZIS and LDH. The inset of Fig. 1e also displays the close integration between LDH and ZIS.

AFM analysis (Fig. 1f-h, Fig. S5) shows the thickness of NiCoFe-LDH@ZIS is 37.01 nm, which is much larger than that of pure bulky flower-like ZIS (13.54 nm) and dandelion-like lamellar structured NiCoFe-LDH (24.74 nm). Additionally, the thickness of NiCoFe-LDH@ZIS is smaller than the simple stacking of ZIS and NiCoFe-LDH, demonstrating these two materials are not simply compounded together, but are tightly integrated through intercalation. The simulated 3D structure demonstrates this more clearly. The changes in BET and pore size before and after the synthesis of NiCoFe-LDH@ZIS are tested by N_2 physical adsorption-desorption. In Fig. 1i, the adsorption-desorption curves of all the three materials belong to type IV isotherms [28]. Compared to NiCoFe-LDH, ZIS and NiCoFe-LDH@ZIS form an H3-type hysteresis loop, indicating that they are typical mesoporous materials [29]. In the range of P/P0 < 0.1, the adsorption curves of NiCoFe-LDH and NiCoFe-LDH@ZIS increase sharply with the rise of P/P0, indicating the existence of a large number of micropores [28,29]. The BET of NiCoFe-LDH@ZIS is 143.55 m^2/g and the average pore size is 4.04 nm, which is between the value of NiCoFe-LDH (172.40 m^2/g, 3.24 nm) and ZIS (51.68 m^2/g, 4.96 nm), confirming that ZIS successfully intercalated LDH to form a micro-mesoporous NiCoFe-LDH@ZIS. The HAADF TEM images in Fig. 1j further confirm the 3D penetrating micro-mesoporous morphology of NiCoFe-LDH@ZIS. The elemental mapping images in Fig. 1j-k and Fig. S6 further confirm the uniform spatial distribution of elements after the intercalation of LDH and ZIS. Specifically, the ZIS consists of Zn, In, and S elements while Ni, Co, Fe, and O elements are successfully introduced into ZIS after forming the hybrid of NiCoFe-LDH@ZIS.

The crystal structures of the materials are characterized by XRD analysis. In Fig. S1, the peak positions, peak shapes, and relative intensities match with the XRD patterns simulated by the software, confirming the successful preparation of pure phases of ZIF-67 [30]. The XRD diffraction peaks of the prepared flower-like bulky ZIS (Fig. 2b) match with the hexagonal ZIS phase (JCPDS No.65-2023). After in situ
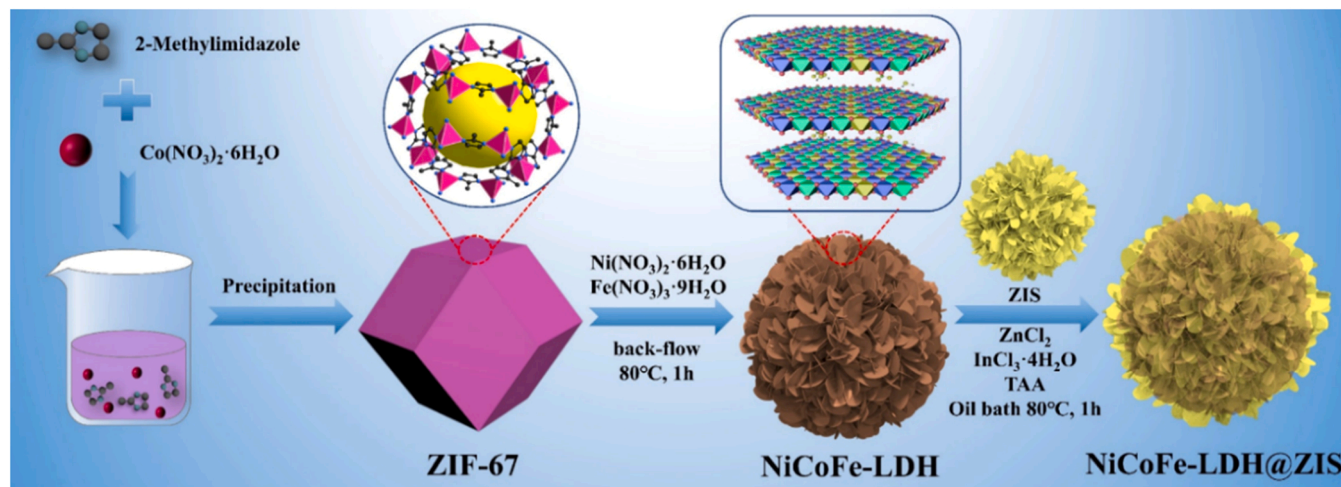
Scheme 1. The schematic synthetic route of 3D penetrating structured micro-mesoporous NiCoFe-LDH@ZIS Z-scheme heterojunction.
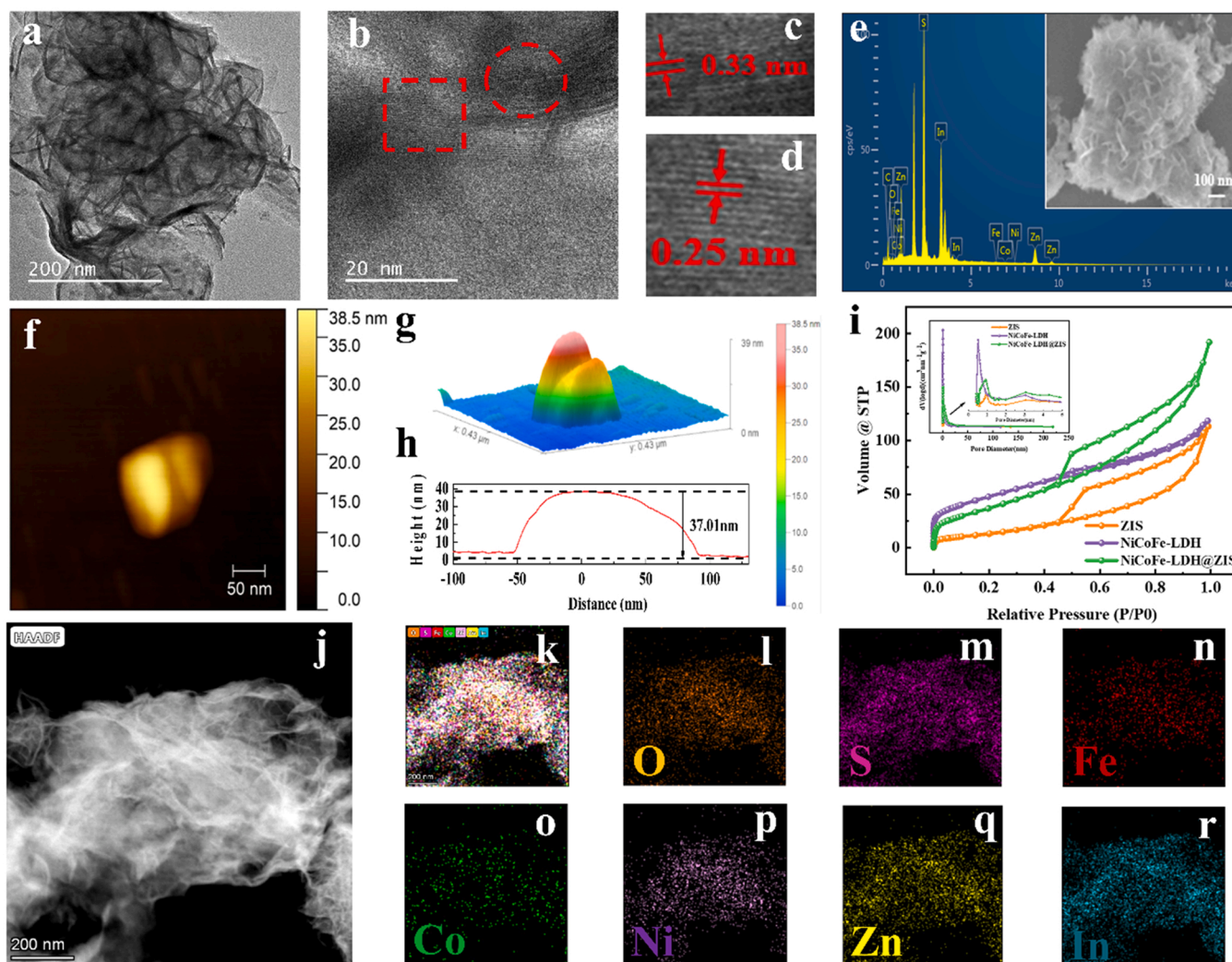
Fig. 1. (a) TEM and (b-d) HRTEM micrographs of NiCoFe-LDH@ZIS, (c) and (d) are the enlarged HRTEM micrographs of the circle and box in (b), (e) EDS spectra, inset of (e) is SEM image, (f-h) AFM image, simulate 3D view and height profile of NiCoFe-LDH@ZIS, (i) N_2 adsorption−desorption isotherm, inset of (i) is pore size distributions of ZIS, NiCoFe-LDH, and NiCoFe-LDH@ZIS, (j) HAADF and (k-r) elemental mapping images of NiCoFe-LDH@ZIS.

etching of ZIF-67, the XRD patterns show diffraction peaks at 11.4°, 34.2° and 60.6°, which are corresponding to (003), (012), and (110) planes of LDH (JCPDS No.51-0463), indicating the formation of NiCoFe-LDH (Fig. 2c) [31]. In detail, the two strong peaks (28.1° and 47.5°) correspond to (102) and (110) crystal planes of ZIS, respectively [17]. The above major diffraction peaks of ZIS also appear in NiCoFe-LDH@ZIS, demonstrating the combination of NiCoFe-LDH@ZIS without altering the structure of ZIS. Relatively weak characteristic patterns of LDH appear in NiCoFe-LDH@ZIS, which may be related to the low percentage of Ni, Co, and Fe elements. This suggestion is also verified by the TEM mapping and EDS patterns.

Fig. 2d shows the FT-IR spectra of ZIS, NiCoFe-LDH, and NiCoFe-LDH@ZIS. The strong peaks of all the samples around 1390, 1630, and 3440 cm^{-1} are associated with hydroxyl groups and surface-adsorbed OH [32]. The low-frequency bands from 500 to 900 cm^{-1} correspond to metal−oxygen (M-O), O-M-O, and M-O-M lattice vibrations of NiCoFe-LDH [33]. The FT-IR spectrum of NiCoFe-LDH@ZIS maintains the main characteristic peaks of ZIS and NiCoFe-LDH, which indicates that the successful intercalation of ZIS into NiCoFe-LDH makes strong electrostatic bonds between them [32,33]. It is crucial in the transfer and cooperative interaction of photogenerated carriers and results in improved PHE activity [34]. The Raman spectra of ZIS, NiCoFe-LDH, and NiCoFe-LDH@ZIS were investigated to further

explore the changes in the surface of samples (Fig. 2e). The peak at 122 cm^{-1} reveals ZIS's layered structure [35]. The other two peaks at approximately 241 and 344 cm^{-1} could be attributed to the LO_1 and LO_2 optical modes of the ZIS, respectively [36]. The peak intensity of NiCoFe-LDH@ZIS increased to some extent and without significant shift compared with ZIS, indicating the maintenance of the original structural features. For NiCoFe-LDH, the peak from 450 to 550 cm^{-1} is mainly attributed to NiOOH [37]. All the samples show an obvious characteristic peak at 474 cm^{-1}, which fully proves the tight binding of NiCoFe-LDH with ZIS. The EPR signal intensities at 2.00 of g (Fig. 2f) show that NiCoFe-LDH@ZIS possesses a higher concentration of S vacancies than ZIS [17]. Additionally, the presence of S vacancies in NiCoFe-LDH@ZIS is also determined by comparing the atomic proportions. Specifically, the amounts of S, In and Zn in photocatalysts are accurately analyzed by ICP-MS and EDS. The atomic ratio of Zn, In and S in NiCoFe-LDH@ZIS is 1: 1.6: 2.9 and ZIS is 1: 1.6: 3.5, further implying the loss of S elements in NiCoFe-LDH@ZIS. The above characterizations synergistically demonstrate the presence of S vacancies in NiCoFe-LDH@ZIS, implying the generation of S vacancies from the intercalation between ZIS and LDH [38].

The elemental composition and surface chemical states of NiCoFe-LDH@ZIS, ZIS, and NiCoFe-LDH are exhibited in the XPS spectra in Fig. 2g-i and Fig. S7. The full XPS spectrum of Fig. S7a shows the
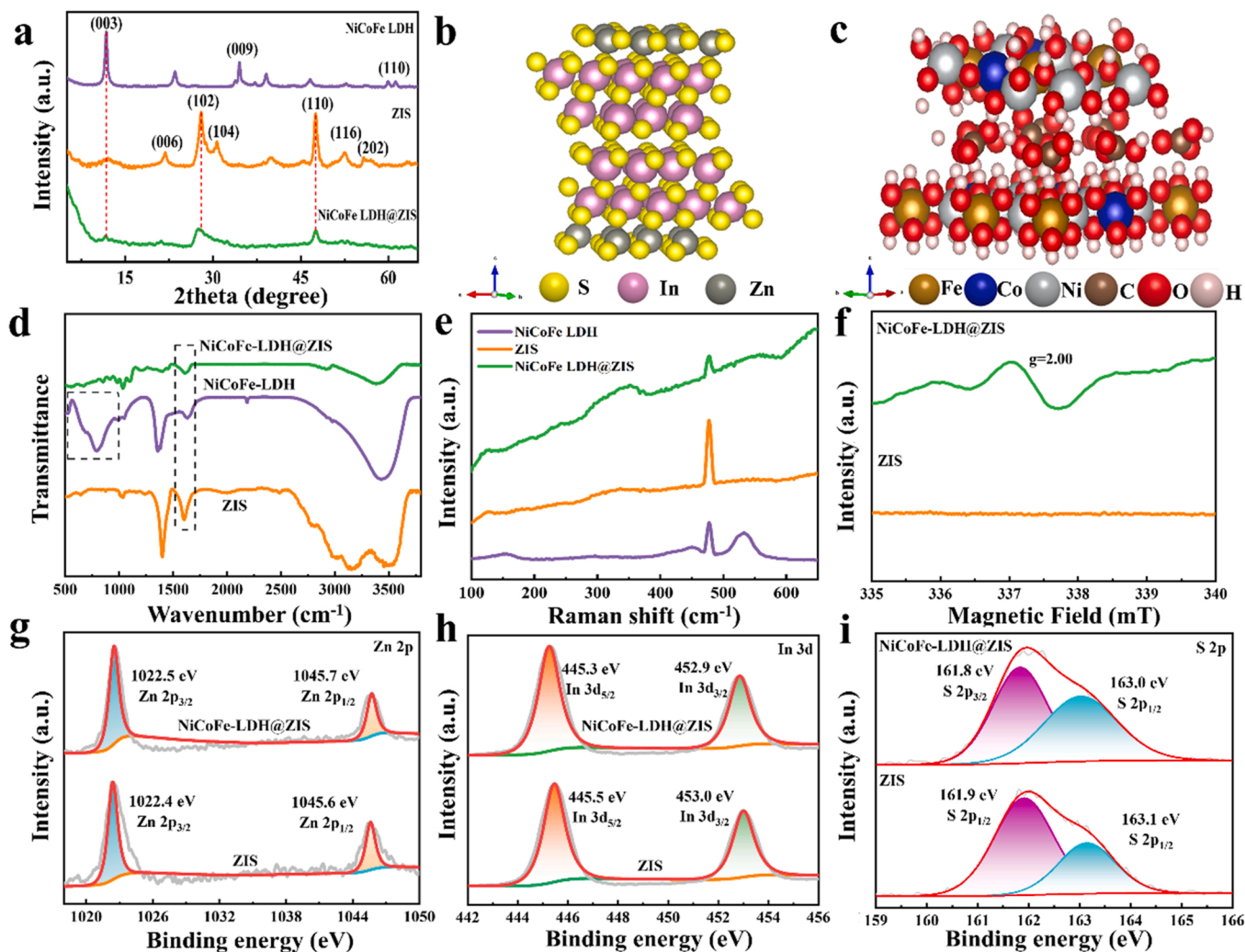
Fig. 2. (a) XRD patterns of ZIS, NiCoFe-LDH and NiCoFe-LDH@ZIS. Schematic structure of (b) ZIS and (c) NiCoFe-LDH. (d) FT-IR and (e) Raman spectra for ZIS, NiCoFe-LDH and NiCoFe-LDH@ZIS. (f) EPR and (g-i) XPS spectra for ZIS and NiCoFe-LDH@ZIS.

elemental composition of NiCoFe-LDH@ZIS, ZIS, and NiCoFe-LDH. Fig. 2g-i display the XPS spectra of Zn 2p, In 3d and S 2p for bulky flower-like ZIS and 3D penetrating micro-mesoporous NiCoFe-LDH@ZIS Z-scheme heterojunction. In Fig. 2g, the binding energy of ZIS at 1022.4 eV and 1045.6 eV are attributed to Zn $2p_{3/2}$ and Zn $2p_{1/2}$, respectively [39]. Zn $2p_{3/2}$ and Zn $2p_{1/2}$ of the NiCoFe-LDH@ZIS sample shifted toward the high binding energy. The two peaks at 445.3 eV and 452.9 eV are attributed to In $3d_{5/2}$ and In $3d_{3/2}$ in NiCoFe-LDH@ZIS (Fig. 2h), which are slightly lower than 445.5 eV and 453.0 eV in ZIS [17]. In Fig. 2i, the binding energy of S 2p in NiCoFe-LDH@ZIS (161.8 eV and 163.0 eV) are lower and weaker compared to ZIS (161.9 eV and 163.1 eV), suggesting the presence of S vacancies in the structure due to low-coordination S [39]. The XPS spectra in Fig. S7 exhibit the peaks of O 1 s and Ni 2p of NiCoFe-LDH@ZIS, both of them shift to higher binding energies according to the fitting analysis. Specifically, Ni-S bonds appear at 851.1 eV only in NiCoFe-LDH@ZIS. Consequently, great shifts are observable in XPS spectra of electron binding energy of Zn 2p, S 2p, and In 3d, demonstrating the existence of charge transfer between NiCoFe-LDH and ZIS [17,39].

The photocatalytic activity of NiCoFe-LDH@ZIS is evaluated by PHE and benzylamine oxidation coupling simultaneously. The reaction is carried out in a mixture of acetonitrile, benzylamine, and water under visible light irradiation. Controlled experiments indicate no photocatalytic product generated in the absence of light irradiation or photocatalysts, proving the reaction is indeed driven by photocatalysis

(Fig. 3a-b). The PHE performance of NiCoFe-LDH@ZIS is substantially improved to 113.57 mmol g^{-1} h^{-1}, which is about 6.24 times higher than the bulky flower-like ZIS (18.19 mmol g^{-1} h^{-1}) and 82.30 times of dandelion-like NiCoFe-LDH (1.38 mmol g^{-1} h^{-1}). Furthermore, the ratio of ZIS in NiCoFe-LDH@ZIS was optimized to improve the bifunctional photocatalytic performance. There is a trade-off effect between the ZIS loading and PHE efficiency (Fig. S8a-b). And the optimized photocatalytic performance is achieved by utilizing a photocatalyst with a 1:10 ratio of NiCoFe-LDH to ZIS. Additionally, the superior hydrogen production cocatalyst (Pt) is introduced into the photocatalytic system to further optimize the PHE performance by photo-deposition process (Fig. S8c-d). The products of benzylamine oxidation coupling are measured by the GC-MS spectrum after irradiation for 8 h (Fig. 3c-d). As a result, the products of both NiCoFe-LDH@ZIS and ZIS are complex, including N-benzylidenebenzylamine, 1,2-Diphenyl-1,2-ethanediamine, N-benzylideneamine and benzaldehyde [40]. Among them, N-benzylidenebenzylamine is the most common benzylamine oxidation coupling product, and the most represented product in this experiment, whose corresponding mass spectra is shown in Fig. S9. The benzylamine conversion and the selectivity of N-benzylidenebenzylamine of NiCoFe-LDH@ZIS are compared with bulky ZIS catalysts. The results show that the conversion of benzylamine of NiCoFe-LDH@ZIS is 97.78 % and the selectivity of N-benzylidenebenzylamine is 80.72 %, which are much greater than that of pristine ZIS at 65.30 % and 38.45 %.

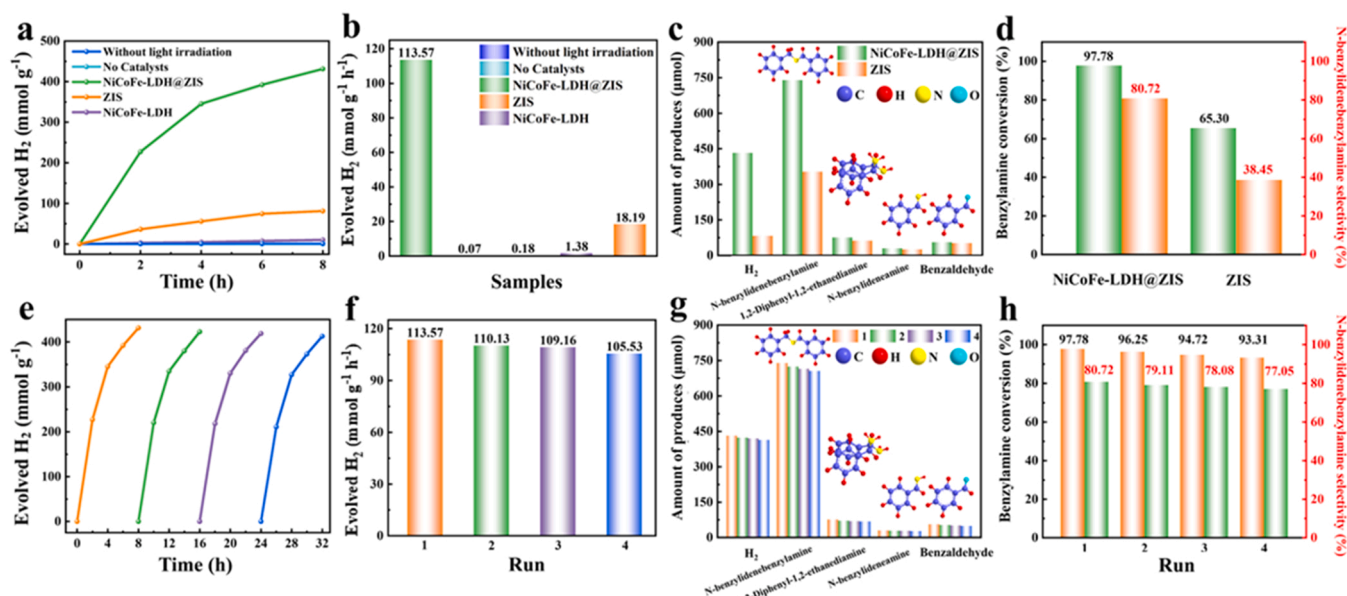In addition, the photocatalytic stability of NiCoFe-LDH@ZIS for the

Fig. 3. (a-b) PHE performances of NiCoFe-LDH@ZIS, NiCoFe-LDH and ZIS and comparable controls without catalysts or light irradiation. (c-d) Product analysis of NiCoFe-LDH@ZIS and ZIS in the bifunctional photocatalytic process. (e-f) Photocatalytic PHE stability test of NiCoFe-LDH@ZIS. (g-h) Product analysis of NiCoFe-LDH@ZIS after photocatalytic stability test.

bifunctional photocatalytic process of PHE and benzylamine oxidation coupling is investigated after four photocatalytic cycles. As shown in Fig. 3e-h, the PHE performance of NiCoFe-LDH@ZIS was almost unchanged after four cycles. And the product species of benzylamine oxidative coupling after four cycles of reaction are consistent. The

benzylamine conversions all maintained at the level of more than 93 %, and the selectivity of N-benzylidenebenzylamine is greater than 77 %. This superior stability is due to the special 3D penetrating micromesoporous structure of the NiCoFe-LDH@ZIS, which enables fuller contact between the catalysts and the reaction substrates, allowing
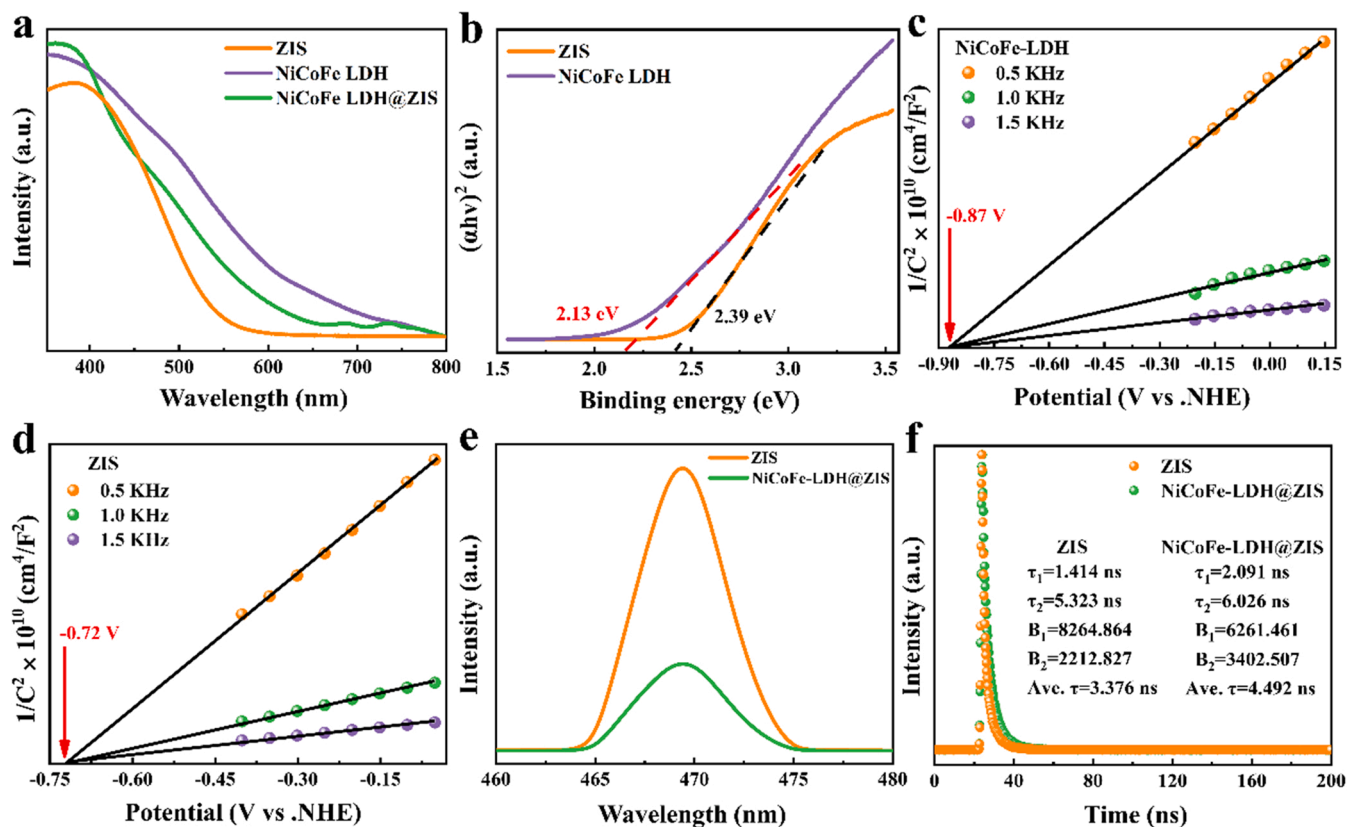

Fig. 4. (a) UV−vis DRS of NiCoFe-LDH@ZIS, NiCoFe-LDH and ZIS. (b) The tauc plots of NiCoFe-LDH and ZIS. (c-d) The Mott–Schottky (MS) curves of NiCoFe-LDH and ZIS. (e) PL and (f) TRPL spectra of NiCoFe-LDH and ZIS.

facilitated mass transfer to avoid clogging and full utilization of the active centers. The multiple refractions of light in the 3D penetrating micro-mesoporous pores promote light utilization efficiency [41]. In addition, the introduction of S vacancies and Z-scheme heterojunctions can accelerate the charge separation, and suppress the combination of PEHP, resulting in more photogenerated charges participating in the reaction [20]. Notably, NiCoFe-LDH@ZIS reaches an impressive 14.31 % AQY at 420 nm monochromatic light, and the PHE performance of the NiCoFe-LDH@ZIS in this work is also relatively prominent compared to the recently reported LDH-based and ZIS-based photocatalysts (Fig. S10, Table S1).

UV–vis diffuse reflectance spectra (DRS) are used to examine the light-harvesting capabilities of samples. In Fig. 4a, the light absorption intensity of NiCoFe-LDH@ZIS is remarkably increased in the full wavelength range when compared to ZIS. To further reveal the mechanism of the enhanced PHE performance, the energy band positions of each component are calculated by combining the Tauc curves (Fig. 4b) and Mott-Schottky (MS) curves (Fig. 4c-d). NiCoFe-LDH and ZIS are n-type semiconductors because of the positive slopes in the MS curves [42,43]. The band gap values E_g corresponding to NiCoFe-LDH and ZIS are 2.13 and 2.39 eV, and the flat-band potentials are -0.87 and -0.72 V (vs NHE). Thus, the conduction bands (E_{CB}) of NiCoFe-LDH and ZIS are about -0.97 and -0.82 V (vs NHE) [42]. The valence bands (E_{VB}) of NiCoFe-LDH and ZIS are about 1.16 and 1.57 V (vs NHE) based on $E_g = E_{VB} - E_{CB}$, respectively.

The interfacial charge transfer properties of NiCoFe-LDH@ZIS and ZIS are investigated by photoluminescence (PL) spectra. In Fig. 4e, the PL intensity of NiCoFe-LDH@ZIS is much lower than ZIS, indicating that the recombination of its PEHP is suppressed, resulting in higher efficiency of carrier separation [40]. This may be caused by S vacancies can trap the photoexcited charges to promote charge separation [44]. Moreover, an inner electron transport pathway is formed based on the heterojunction structure and strong interaction between NiCoFe-LDH and ZIS, which also leads to a further reduced fluorescence signal [45]. The average fluorescence lifetime of photocatalysts is investigated by time-resolved photoluminescence (TRPL) spectroscopy (Fig. 4f).

According to results calculated based on Ave. $\tau = (B_1\tau_1^2 + B_2\tau_2^2)/(B_1\tau_1 + B_2\tau_2)$, the average fluorescence lifetime of NiCoFe-LDH@ZIS (4.49 ns) is longer than ZIS (3.38 ns) [9]. Consequently, S vacancies and heterojunction structure indeed facilitate the photogenerated charge separation and result in improved photocatalytic activity [44].

The optimization of photogenerated carrier migration and separation of the 3D penetrating micro-mesoporous NiCoFe-LDH@ZIS Z-scheme heterojunction is further investigated by photoelectrochemical characterization. In EIS spectra (Fig. 5a), the Nyquist plots of NiCoFe-LDH@ZIS exhibit a much smaller semicircle at a higher frequency than other controls, indicating the superior charge transfer resistance (Rct) [46]. Furthermore, the transient photocurrent responses of the catalysts are performed to further identify the charge separation properties. NiCoFe-LDH@ZIS exhibits higher photocurrent density than pure NiCoFe-LDH and ZIS (Fig. 5b), indicating accelerated separation and transport of photogenerated carriers [9]. At the same time, photocurrent responses are highly reproducible and remain stable. To further visualize photo-generated carriers, a laser confocal fluorescent microscopy (LCFM) is performed. As shown in Fig. 5c-f, fluorescent images and interactive 3D surface plots all indicate that the fluorescence intensity of ZIS is higher than NiCoFe-LDH@ZIS. The existence of S vacancies in heterogeneous NiCoFe-LDH@ZIS reduces the fluorescence intensity of NiCoFe-LDH@ZIS. Therefore, S vacancies can improve the charge separation and transport efficiency of NiCoFe-LDH@ZIS, which in turn enhances the performance of photocatalysis [17].

In order to clarify the mechanism of the reaction, the main active species in the reaction process are investigated by quenching experiments. Several quenchers including triethanolamine (TEOA) for h^+, $K_2S_2O_8$ for e^-, p-benzoquinone (BQ) for $\cdot O_2^-$, and tert-butanol (TBA) for $\cdot OH$ are added into the reaction system to study the photocatalytic performance of the NiCoFe-LDH@ZIS (Fig. S11). Consequently, we can infer that $\cdot O_2^-$ radicals and $\cdot OH$ radicals are the active species in the reaction, and photogenerated electrons and holes are the initial driving forces of the reaction. The photocatalytic mechanism of the 3D penetrating-structured micro-mesoporous Z-scheme heterojunction of NiCoFe-LDH@ZIS is further revealed by DFT calculations. Fig. 6a-b
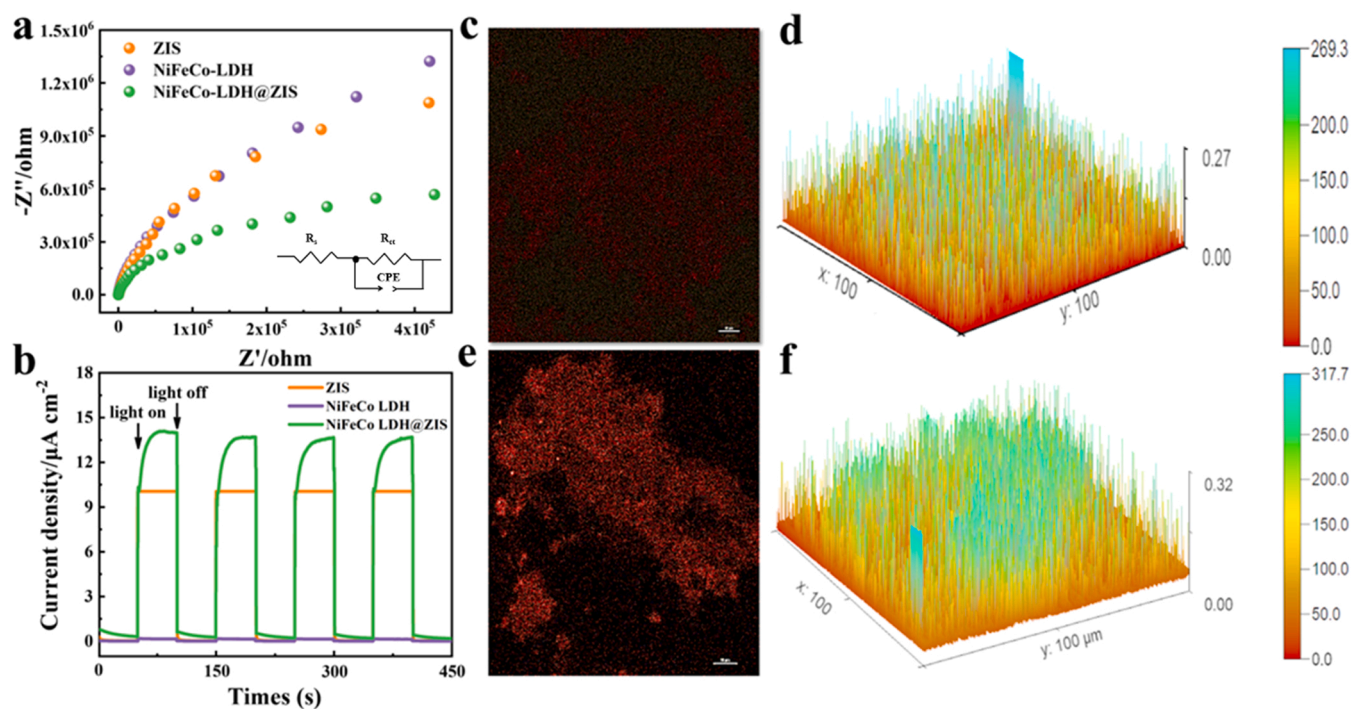

Fig. 5. (a) EIS spectra and (b) Transient photocurrent response spectra of NiCoFe-LDH@ZIS, NiCoFe-LDH and ZIS. (c, e) LCFM image and (d, f) interactive 3D surface plot of NiCoFe-LDH@ZIS and ZIS.
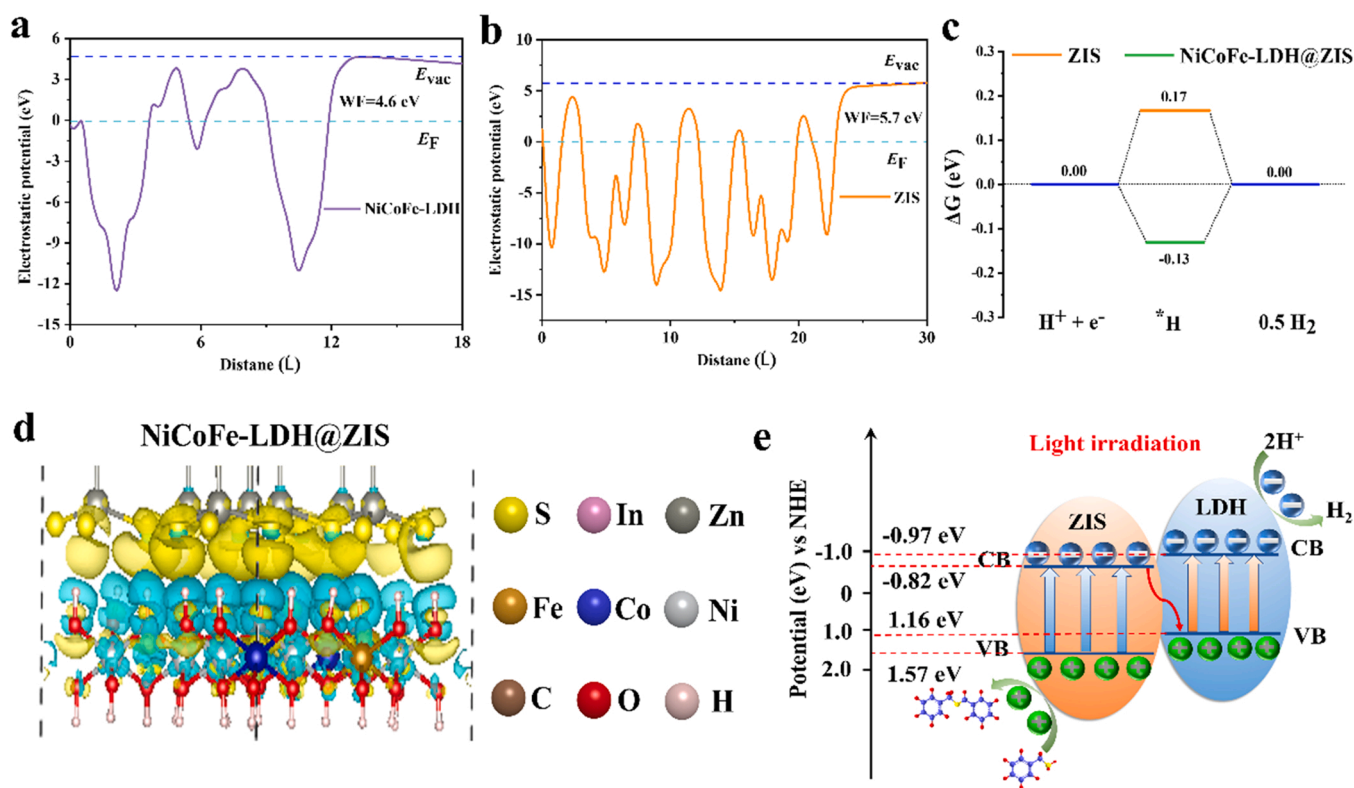
Fig. 6. Electrostatic potential of NiCoFe-LDH (a) and ZIS (b). (c) ΔG calculated for the HER via the *H intermediate on NiCoFe-LDH@ZIS (green line) and ZIS (orange line). (d) Charge density difference for NiCoFe-LDH@ZIS Z-scheme heterojunction. (e) Dual-functional photocatalytic reaction mechanism for PHE and benzylamine oxidation based on NiCoFe-LDH@ZIS Z-scheme heterojunction.

exhibits the surface electrostatic potentials of NiCoFe-LDH (001) and ZIS (002) crystal planes, respectively. The differences in the work function (WF) of NiCoFe-LDH (3.3 eV) and ZIS (6.6 eV) indicate charge transfer at the interface between NiCoFe-LDH and ZIS. The higher WF of ZIS will lead to electron transfer from NiCoFe-LDH to ZIS when they are tightly combined until the Fermi level equilibrium is reached [47]. The band edges of ZIS bent downward due to gaining electrons, while NiCoFe-LDH bends to the opposite direction. Based on the generated built-in electric field in NiCoFe-LDH@ZIS, energy band bending, electrostatic interaction, and Z-scheme heterojunction charge transfer pathway existed between NiCoFe-LDH and ZIS. Specifically, upon irradiation of visible light, the photogenerated electrons on the CB of ZIS combine with the photogenerated holes on the VB of NiCoFe-LDH, while the electrons on the CB of NiCoFe-LDH and the holes on the VB of ZIS are retained for reductive and oxidative reactions, respectively [48]. Ultimately, this charge carrier transportation process greatly improves the redox ability of the NiCoFe-LDH@ZIS catalyst, which further enhances the PHE performance.

To further illustrate the improved PHE performance, Gibbs free energy (ΔG) of the PHE reaction of ZIS and NiCoFe-LDH@ZIS were calculated in Fig. 6c [49]. The binding energy ΔG of *H reaction intermediate (ΔG_{*H}) on ZIS is 0.17 eV. However, NiCoFe-LDH@ZIS (−0.13 eV) is lower than ΔG_{*H} of ZIS and closer to the ideal hydrogen adsorption-free energy of 0 eV. The higher ΔG_{*H} indicates that *H will create a larger energy barrier on the ZIS surface [40]. And the intercalation of ZIS by LDH reduces the energy of *H reaction intermediates energy barrier, thus facilitating the photocatalytic hydrogen generation [50]. As shown in Fig. 6d, a differential charge of NiCoFe-LDH@ZIS Z-scheme heterojunction reveals electronic interaction at interfaces. In detail, the blue and yellow regions represent electron consumption and electron accumulation. These results indicate strong interfacial coupling between NiCoFe-LDH and ZIS, and electron migration conforms to a Z-scheme pathway, which is consistent with the analysis of work

function results [51]. Based on the experimental results and DFT theoretical calculations, the dual-functional photocatalytic reaction mechanism is shown in Fig. 6e. In short, the PEHP are used for PHE and benzylamine oxidation coupling, respectively. Therefore, the bifunctional photocatalytic reaction of PHE and benzylamine oxidation can be realized based on the 3D penetrating micro-mesoporous NiCoFe-LDH@ZIS Z-scheme heterojunction.

4. Conclusion

In summary, a 3D penetrating structured micro-mesoporous NiCoFe-LDH@ZIS Z-scheme heterojunction is constructed for a bifunctional photocatalytic process of simultaneously PHE coupled with oxidation of benzylamine. We experimentally and theoretically demonstrate the spatial separation of both surface redox regions and charge carriers featured by NiCoFe-LDH@ZIS Z-scheme heterojunction. S vacancies and the Z-scheme heterojunction retain the strong redox capacity of PEHP, reduce the energy barrier of surface reaction and improve the charge separation efficiency. Notably, the special 3D penetrating micro-mesoporous structure of the NiCoFe-LDH@ZIS catalysts enables fuller contact between the catalysts and the reaction substrates, allowing greater use of the active centers. The penetration pore can avoid the clogging phenomenon occurring easily after multiple photocatalytic cycles, and multiple refractions of light in the interconnected hierarchical pores can promote light utilization efficiency. The optimized 3D penetrating micro-mesoporous NiCoFe-LDH@ZIS Z-scheme heterojunction exhibits 113.57 mmol g^{-1} h^{-1} PHE rate and 97.78 % conversion rate of benzylamine. Additionally, the selectivity of N-benzylidenebenzylamine is greater than 80 %, and it shows excellent stability after four photocatalytic cycles. This work holds great promise for simultaneous solar-driven hydrogen production and synthesis of high-value organic chemicals.

CRediT authorship contribution statement

Chenxi Tang: Validation, Formal analysis, Investigation, Resources, Data curation, Writing – original draft. **Tengfei Bao:** Validation, Formal analysis, Investigation, Resources, Data curation. **Shuming Li:** Validation, Formal analysis. **Xiuyan Wang:** Investigation, Resources, Data curation. **Heng Rao:** Data curation. **Ping She:** Conceptualization, Validation, Writing – review & editing. **Jun-sheng Qin:** Conceptualization, Writing – review & editing.

Declaration of Competing Interest

The authors declare that they have no known competing financial interests or personal relationships that could have appeared to influence the work reported in this paper.

Data availability

No data was used for the research described in the article.

Acknowledgements

Appendix A. Supporting information

Supplementary data associated with this article can be found in the online version at doi:10.1016/j.apcatb.2023.123384.

References

[1] D. Shindell, C.J. Smith, Climate and air-quality benefits of a realistic phase-out of fossil fuels, Nature 573 (2019) 408–411, https://doi.org/10.1038/s41586-019-1554-z.

[2] J. Gong, C. Li, M.R. Wasielewski, Advances in solar energy conversion, Chem. Soc. Rev. 48 (2019) 1862–1864, https://doi.org/10.1039/C9CS90020A.

[3] H. Liu, C. Xu, D. Li, H.-L. Jiang, Photocatalytic hydrogen production coupled with selective benzylamine oxidation over MOF composites, Angew. Chem. Int. Ed. 57 (2018) 5379–5383, https://doi.org/10.1002/anie.201800320.

[4] C. Han, Y.-H. Li, J.-Y. Li, M.-Y. Qi, Z.-R. Tang, Y.-J. Xu, Cooperative syngas production and C-N bond formation in one photoredox cycle, Angew. Chem. Int. Ed. 60 (2021) 7962–7970, https://doi.org/10.1002/anie.202015756.

[5] Q. Guo, F. Liang, X.-B. Li, Y.-J. Gao, M.-Y. Huang, Y. Wang, S.-G. Xia, X.-Y. Gao, Q.-C. Gan, Z.-S. Lin, C.-H. Tung, L.-Z. Wu, Efficient and selective CO2 reduction integrated with organic synthesis by solar energy, Chem 5 (2019) 2605–2616, https://doi.org/10.1016/j.chempr.2019.06.019.

[6] S. Kampouri, K.C. Stylianou, Dual-functional photocatalysis for simultaneous hydrogen production and oxidation of organic substances, ACS Catal. 9 (2019) 4247–4270, https://doi.org/10.1021/acscatal.9b00332.

[7] N. Luo, T. Montini, J. Zhang, P. Fornasiero, E. Fonda, T. Hou, W. Nie, J. Lu, J. Liu, M. Heggen, L. Lin, C. Ma, M. Wang, F. Fan, S. Jin, F. Wang, Visible-light-driven coproduction of diesel precursors and hydrogen from lignocellulose-derived methylfurans, Nat. Energy 4 (2019) 575–584, https://doi.org/10.1038/s41560-019-0403-5.

[8] Q. Lin, Y.-H. Li, M.-Y. Qi, J.-Y. Li, Z.-R. Tang, M. Anpo, Y.M.A. Yamada, Y.-J. Xu, Photoredox dual reaction for selective alcohol oxidation and hydrogen evolution over nickel surface-modified ZnIn2S4, Appl. Catal. B 271 (2020) 118946, https://doi.org/10.1016/j.apcatb.2020.118946.

[9] Y.Q. He, H. Rao, K.P. Song, J.X. Li, Y. Yu, Y. Lou, C.G. Li, Y. Han, Z. Shi, S.H. Feng, 3D hierarchical ZnIn2S4 nanosheets with rich Zn vacancies boosting photocatalytic CO2 reduction, Adv. Funct. Mater. 29 (2019) 1905153, https://doi.org/10.1002/adfm.201905153.

[10] Z. Lei, W. You, M. Liu, G. Zhou, T. Takata, M. Hara, K. Domen, C. Li, Photocatalytic water reduction under visible light on a novel ZnIn2S4 catalyst synthesized by hydrothermal method, Chem. Commun. 21 (2003) 2142–2143, https://doi.org/10.1039/B306813G.

[11] M. Mata, X. Zhou, F. Furtmayr, J. Teubert, S. Gradečak, M. Eickhoff, A.F. Morral, J. Arbiol, A review of MBE grown 0D, 1D and 2D quantum structures in a nanowire, J. Mater. Chem. C 1 (2013) 4300–4312, https://doi.org/10.1039/C3TC30556B.

[12] Z.T. Hu, Y.N. Liang, J. Zhao, Y.D. Zhang, E.H. Yang, J.M. Chen, T.T. Lim, Ultra-effective integrated technologies for water disinfection with a novel ^{0}D–^{2}D-3D nanostructured rGO-AgNP/Bi2Fe4O9 composite, Appl. Catal. B 227 (2018) 548–556, https://doi.org/10.1016/j.apcatb.2018.01.047.

[13] H.C. Yang, R.Y. Cao, P.X. Sun, J.M. Yin, S.W. Zhang, X.J. Xu, Constructing electrostatic self-assembled 2D/2D ultra-thin ZnIn2S4/protonated g-C3N4 heterojunctions for excellent photocatalytic performance under visible light, Appl. Catal. B 256 (2019), 117862, https://doi.org/10.1016/j.apcatb.2019.117862.

[14] P. Kuang, M. Sayed, J. Fan, B. Cheng, J. Yu, 3D graphene-based H2-production photocatalyst and electrocatalyst, Adv. Energy Mater. 10 (2020), 1903802, https://doi.org/10.1002/aenm.201903802.

[15] H. Zhao, Z.Y. Hu, J. Liu, Y. L, M. Wu, G.V. Tendeloo, B.-L. Su, Blue-edge slow photons promoting visible-light hydrogen production on gradient ternary 3DOM TiO2-Au-CdS photonic crystals, Nano Energy 47 (2018) 266–274, https://doi.org/10.1016/j.nanoen.2018.02.052.

[16] F.S. Xing, Q.W. Liu, C.J. Huang, Mo-doped ZnIn2S4 flower-like hollow microspheres for improved visible light-driven hydrogen evolution, Sol. RRL 4 (2020), 1900483, https://doi.org/10.1002/solr.201900483.

[17] Y.Q. He, C.L. Chen, Y.X. Liu, Y.L. Yang, C.G. Li, Z. Shi, Y. Han, S.H. Feng, Quantitative evaluation of carrier dynamics in full-spectrum responsive metallic ZnIn2S4 with indium vacancies for boosting photocatalytic CO2 reduction, Nano Lett. 22 (2022) 4970–4978, https://doi.org/10.1021/acs.nanolett.2c01666.

[18] S.H. Wang, Z.R. Li, G.D. Yang, Y.B. Xu, Y.Y. Zheng, S.X. Zhong, Y.L. Zhao, S. Bai, Embedding nano-piezoelectrics into heterointerfaces of S-scheme heterojunctions for boosting photocatalysis and piezophotocatalysis, Small (2023), 2302717, https://doi.org/10.1002/smll.202302717.

[19] J.X. Low, B.Z. Dai, T. Tong, C.J. Jiang, J.G. Yu, In situ irradiated X-Ray photoelectron spectroscopy investigation on a direct Z-Scheme TiO2/CdS composite film photocatalyst, Adv. Mater. 31 (2019), 1802981, https://doi.org/10.1002/adma.201807920.

[20] P.L. Wang, S.Y. Fan, X.Y. Li, J. Wang, Z.Y. Liu, C.P. Bai, M.O. Tadé, S.M. Liu, Piezotronic effect and hierarchical Z-scheme heterostructure stimulated photocatalytic H2 evolution integrated with C-N coupling of benzylamine, Nano Energy 89 (2021), 106349, https://doi.org/10.1016/j.nanoen.2021.106349.

[21] G. Yang, H. Ding, D.M. Chen, J.J. Feng, Q. Hao, Y.F. Zhu, Construction of urchin-like ZnIn2S4-Au-TiO2 heterostructure with enhanced activity for photocatalytic hydrogen evolution, Appl. Catal. B 234 (2018) 260–267, https://doi.org/10.1016/j.apcatb.2018.04.038.

[22] Y. Dong, D.Q. Wei, R. He, R.S. Yuan, T.F. Xie, Z.H. Li, Rational design of Z-scheme PtS-ZnIn2S4/WO3-MnO2 for overall photo-catalytic water splitting under visible light, Appl. Catal. B 258 (2019) 117948, https://doi.org/10.1016/j.apcatb.2019.117948.

[23] Q. Niu, M. Yang, D. Luan, N.W. Li, L. Yu, X.W. Lou, Construction of Ni-Co-Fe hydr (oxy)oxide@Ni-Co layered double hydroxide yolk-shelled microrods for enhanced oxygen evolution, Angew. Chem. Int. Ed. 61 (2022), e202213049, https://doi.org/10.1002/anie.202213049.

[24] S. Zhao, Q. Liang, W. Gao, M. Zhou, C. Yao, S. Xu, Z.Y. Li, In situ growth of ZnIn2S4 on MOF-derived Ni–Fe LDH to construct ternary-shelled nanotubes for efficient photocatalytic hydrogen evolution, Inorg. Chem. 60 (2021) 9762–9772, https://doi.org/10.1021/acs.inorgchem.1c01064.

[25] S. Zhang, Y.X. Zhao, S. Run, Z. Chao, G.I.N. Waterhouse, L.-Z. Wu, C.-H. Tung, T. R. Zhang, Efficient photocatalytic nitrogen fixation over Cu$^{δ+}$-modified defective ZnAl-layered double hydroxide nanosheets, Adv. Energy Mater. 10 (2020) 1901973, https://doi.org/10.1002/aenm.201901973.

[26] Z.F. Yang, S.J. Li, X.N. Xia, Y.T. Liu, Hexagonal MgAl-LDH simultaneously facilitated active facet exposure and holes storage over ZnIn2S4/MgAl-LDH heterojunction for boosting photocatalytic activities and anti-photocorrosion, Sep. Purif. Technol. 300 (2022), 121819, https://doi.org/10.1016/j.seppur.2022.121819.

[27] H. Masuda, K. Fukuda, Ordered metal nanohole arrays made by a two-step replication of honeycomb structures of anodic alumina, Science 268 (1995) 1466–1468, https://doi.org/10.1126/science.268.5216.146.

[28] U.K. Nizar, J. Efendi, L. Yuliati, D. Gustiono, H. Nur, A new way to control the coordination of titanium (IV) in the sol–gel synthesis of broom fibers-like mesoporous alkyl silica–titania catalyst through addition of water, Chem. Eng. J. 222 (2013) 23–31, https://doi.org/10.1016/j.cej.2013.02.053.

[29] T.C. Zhao, A. Elzatahry, X.M. Li, D.Y. Zhao, Single-micelle-directed synthesis of mesoporous materials, Nat. Rev. Mater. 4 (2019) 775–791, https://doi.org/10.1038/s41578-019-0144-x.

[30] H. Hu, L. Han, M.Z. Yu, Z.Y. Wang, X.W. Lou, Metal–organic-framework-engaged formation of Co nanoparticle-embedded carbon@Co9S8 double-shelled nanocages for efficient oxygen reduction, Energy Environ. Sci. 9 (2016) 107–111, https://doi.org/10.1039/C5EE02903A.

[31] Y.P. Lin, H. Wang, C.-K. Peng, L.M. Bu, C.-L. Chiang, K. Tian, Y. Zhao, J.Q. Zhao, Y.-G. Lin, J.-M. Lee, L.J. Gao, Co-induced electronic optimization of hierarchical NiFe LDH for oxygen evolution, Small 16 (2020), 2002426, https://doi.org/10.1002/smll.202002426.

[32] W.-K. Jo, S. Moru, S. Tonda, A green approach to the fabrication of a TiO2/NiAl-LDH core–shell hybrid photocatalyst for efficient and selective solar-powered reduction of CO2 into value-added fuels, J. Mater. Chem. A 8 (2020) 8020–8032, https://doi.org/10.1039/D0TA00104J.

[33] S. Nayak, L. Mohapatra, K. Parida, Visible light-driven novel g-C3N4/NiFe-LDH composite photocatalyst with enhanced photocatalytic activity towards water oxidation and reduction reaction, J. Mater. Chem. A 3 (2015) 18622–18635, https://doi.org/10.1039/C5TA05002B.

[34] Y.D. Sun, X.P. Wang, Q. Fu, C.X. Pan, Construction of direct Z-Scheme heterojunction NiFe-layered double hydroxide (LDH)/$Zn_{0.5}Cd_{0.5}S$ for photocatalytic H_2 evolution, ACS Appl. Mater. Interfaces 13 (2021) 39331–39340, https://doi.org/10.1021/acsami.1c09650.

[35] M.-Q. Yang, Y.-J. Xu, W.H. Lu, K.Y. Zeng, H. Zhu, Q.-H. Xu, G.W. Ho, Self-surface charge exfoliation and electrostatically coordinated 2D hetero-layered hybrids, Nat. Commun. 8 (2017) 14224, https://doi.org/10.1038/ncomms14224.

[36] Y.W. Zhu, L.L. Wang, Y.T. Liu, L.H. Shao, X.N. Xia, In-situ hydrogenation engineering of $ZnIn_2S_4$ for promoted visible-light water splitting, Appl. Catal. B 241 (2019) 483–490, https://doi.org/10.1016/j.apcatb.2018.09.062.

[37] M.M. Cai, Q. Zhu, X.Y. Wang, Z.Y. Shao, L. Yao, H. Zeng, X.F. Wu, J. Chen, K.K. Huang, S.H. Feng, Formation and stabilization of NiOOH by introducing α-FeOOH in LDH: composite electrocatalyst for oxygen evolution and urea oxidation reactions, Adv. Mater. 35 (2022), 2209338, https://doi.org/10.1002/adma.202209338.

[38] C. Du, Q. Zhang, Z.Y. Lin, B. Yan, C.X. Xia, G.W. Yang, Half-unit-cell $ZnIn_2S_4$ monolayer with sulfur vacancies for photocatalytic hydrogen evolution, Appl. Catal. B 248 (2019) 193–201, https://doi.org/10.1016/j.apcatb.2019.02.027.

[39] X.L. Liu, D.J. Dai, Z.H. Cui, Q.Q. Zhang, X.Q. Gong, Z.Y. Wang, Y.Y. Liu, Z.K. Zheng, H.F. Cheng, Y. Dai, B.B. Huang, P. Wang, Optimizing the reaction pathway by active site regulation in the CdS/Fe_2O_3 Z-Scheme heterojunction system for highly selective photocatalytic benzylamine oxidation integrated with H_2 production, ACS Catal. 12 (2022) 12386–12397, https://doi.org/10.1021/acscatal.2c03550.

[40] P. Zhang, X.W. Lou, Design of hetero structured hollow photocatalysts for solar-to-chemical energy conversion, Adv. Mater. 31 (2019), 1900281, https://doi.org/10.1002/adma.201900281.

[41] G.P. Zhang, X.W. Zhu, D.Y. Chen, N.J. Li, Q.F. Xu, H. Li, J.H. He, H. Xu, J.M. Lu, Hierarchical *Z*-scheme g-C_3N_4/Au/$ZnIn_2S_4$ photocatalyst for highly enhanced visible-light photocatalytic nitric oxide removal and carbon dioxide conversion, Environ. Sci. Nano 7 (2020) 676–687, https://doi.org/10.1039/C9EN01325C.

[42] S.B. Wang, B.Y. Guan, Y. Lu, X.W. Lou, Formation of hierarchical In_2S_3–$CdIn_2S_4$ hetero structured nanotubes for efficient and stable visible light CO_2 reduction, J. Am. Chem. Soc. 139 (2017) 17305–17308, https://doi.org/10.1021/jacs.7b10733.

[43] L. Lei, Z.D. Qin, L. Ries, S. Hong, T. Michel, J. Yang, C. Salameh, M. Bechelany, P. Miele, D. Kaplan, M. Chhowalla, D. Voiry, Role of sulfur vacancies and undercoordinated Mo regions in MoS_2 nanosheets toward the evolution of hydrogen, ACS Nano 13 (2019) 6824–6834, https://doi.org/10.1021/acsnano.9b01583.

[44] S.Q. Zhang, Z.F. Zhang, Y.M. Si, B. Li, F. Deng, L.X. Yang, X. Liu, W.L. Dai, S.L. Luo, Gradient hydrogen migration modulated with self-adapting S vacancy in copper-doped $ZnIn_2S_4$ nanosheet for photocatalytic hydrogen evolution, ACS Nano 15 (2021) 15238–15248, https://doi.org/10.1021/acsnano.1c05834.

[45] Y.Z. Wei, N.L. Yang, K.K. Huang, J.W. Wan, F.F. You, R.B. Yu, S.H. Feng, D. Wang, Steering hollow multi shelled structures in photocatalysis: optimizing surface and mass transport, Adv. Mater. 32 (2020), 2002556, https://doi.org/10.1002/adma.202002556.

[46] J.J. Liu, B. Cheng, J.G. Yu, A new understanding of the photocatalytic mechanism of the direct Z-scheme g-C_3N_4/TiO_2 heterostructure, Phys. Chem. Chem. Phys. 18 (2016) 31175–31183, https://doi.org/10.1039/C6CP06147H.

[47] J.W. Fu, Q.L. Xu, J.X. Low, C.J. Jiang, J.G. Yu, Ultrathin 2D/2D WO_3/g-C_3N_4 step-scheme H_2-production photocatalyst, Appl. Catal. B 243 (2019) 556–565, https://doi.org/10.1016/j.apcatb.2018.11.011.

[48] F.H. Ma, S.H. Wang, L.Y. Han, Y.H. Guo, Z.Y. Wang, P. Wang, Y.Y. Liu, H.F. Cheng, Y. Dai, Z.K. Zheng, B.B. Huang, Targeted regulation of the electronic states of nickel toward the efficient electrosynthesis of benzonitrile and hydrogen production, ACS Appl. Mater. Interfaces 13 (2021) 56140–56150, https://doi.org/10.1021/acsami.1c16048.

[49] P.L. Wang, S.Y. Fan, X.Y. Li, J. Wang, Z.Y. Liu, Z.D. Niu, M.O. Tadé, S.M. Liu, Single Pd atoms synergistically manipulating charge polarization and active sites for simultaneously photocatalytic hydrogen production and oxidation of benzylamine, Nano Energy 95 (2022), 107045, https://doi.org/10.1016/j.nanoen.2022.107045.

[50] S.T. Bao, Q.Y. Tan, S.D. Wang, J. Guo, K.L. Lv, S.A.C. Carabineiro, L.L. Wen, TpBD COF@$ZnIn_2S_4$ nanosheets: a novel S-scheme heterojunction with enhanced photoreactivity for hydrogen production, Appl. Catal. B 330 (2023), 122624, https://doi.org/10.1016/j.apcatb.2023.122624.

[51] B. Hinnemann, P.G. Moses, J. Bonde, K.P. Jørgensen, J.H. Nielsen, S. Horch, I. Chorkendorff, J.K. Nørskov, Biomimetic hydrogen evolution: MoS_2 nanoparticles as catalyst for hydrogen evolution, J. Am. Chem. Soc. 127 (2005) 5308–5309, https://doi.org/10.1021/ja0504690.